https://doi.org/10.5194/egusphere-2026-4453
Preprint. Discussion started: 12 August 2026

Meso to sub-mesoscale origins of strong surface winds and influence of surface waves in an extra-tropical cyclone

Sophia E. Brumer[1], Florian Pantillon[1], Joris Pianezze[1], and Nicolas Maury[1]
[1]LAERO, Université de Toulouse, CNRS, IRD, Toulouse, France
Correspondence: Sophia E. Brumer (sophia.brumer@cnrs.fr)

Abstract. Extra-tropical cyclones can bring extreme surface winds. Several mesoscale jets can be associated with these winds originating from the upper, mid, and lower troposphere. Sub-mesoscale processes have been shown to play a major role in the downward transport of jets, but few modeling studies represent them explicitly. This study sheds light in the relative contribution and storm-relative location of jets present in the explosive cyclone Alex which made landfall in southern Brittany in October 2020 causing extensive wind damage in Belle-Ile and further inland. A series of stand-alone atmospheric simulations and coupled wave-atmosphere simulations using the Meso-NH and WAVEWATCH-III® models were run. Their horizontal grid spacing was incrementally halved by two going from 1.6 km (numerical weather prediction mode) down to 100 m (large eddy simulation mode). The simulated storm is consistent across resolutions at the mesoscale with little differences in extreme wind values between the kilometric and hectometric resolutions. Waves coupling is shown to decrease surface wind extremes by 0.5 to 1.5 $\mathrm{m\,s^{-1}}$. Impacts on the surface drag coefficient and winds are not uniform spatially with winds decreasing ahead of the cold front and within the high wind core while decreasing elsewhere. Online trajectory calculations allow for a Lagrangian air mass tracking in Meso-NH. In the kilometric simulation, four distinct jets are shown to be responsible for the strongest winds. The evolution of state parameters along these trajectories helps match the jets to the classical conceptual model for extra-tropical cyclones. Evidence hints to the presence of a Sting Jet associated with Alex's extreme winds, along with the more common Cold Conveyor Belt, and Dry Intrusion. The fourth jet is labeled as Potential Sting Jet on account of its similarities with the Sting Jet prior to subsidence. The Cold Jet is shown to be responsible not only for the majority of the strong wind trajectories in the lower 500 m, but also for the strongest wind speeds. Spatial distributions of these jets is further investigated in the hectometric simulation. These reveal that the Sting Jet descends towards the surface at the rear of the high wind core in the frontal fracture region. This location differs from that reported for previously studied storms where the sting jets are typically found at the forefront of the high wind core. Two distinct Dry Jets are shown to coexist, one descending to the surface around the Sting Jet and another one remaining above the Cold Jet. The Potential Sting Jet is located above the cold conveyor belt and shown to be brought down towards the lower troposphere by coherent structures invigorated by moist processes and spanning several kilometers in width and height at the outer edge of the cloud head. Unlike in previous high-resolution numerical studies, boundary layer rolls are not found to play a key role at the studied instant. Different sting jet location and processes associated with potential sting jet subsidence compared to literature, encourage more systematic studies of extra-topical cyclones through common diagnostics adapted for both kilometric and hectometric resolutions.

https://doi.org/10.5194/egusphere-2026-4453
Preprint. Discussion started: 12 August 2026

1 Introduction

While extra-tropical cyclones are essential components of the weather, climate and water cycle in the mid-latitudes, the associated windstorms are widespread meteorological hazards. In the northern hemisphere they often occur in regions located close to the Pacific and Atlantic storm tracks such as western (Mass and Dotson, 2010) and eastern North America (Bentley et al., 2019). Over Europe, windstorms belong to the most destructive natural hazards and are the topic of intense fundamental and applied research (Pinto et al., 2019). Extra-tropical cyclones have been investigated for more than one century and their dynamics are well understood at the synoptic scale (Schultz et al., 2018). At the mesoscale, a commonly accepted description relies on the conveyor belt model that describes coherent airflows within cyclones (Carlson, 1980). The principal airflows are the Warm Conveyor Belt (WCB) that ascends polewards from lower to upper levels, the Cold Conveyor Belt (CCB) that rotates around the cyclone center at lower levels, and the dry intrusion (DI) that descends from upper levels. Surface winds have been attributed to the different airflows during the life cycle of extra-tropical cyclones that reach northwestern Europe (Hewson and Neu, 2015).

Some intense maritime cyclones developing a bent-back front further involve an additional airflow that may result in the strongest winds: the Sting Jet (SJ) first documented by Browning (2004). The SJ originates from mid levels but, unlike the DI, descends from the cloud head above the CCB and into the frontal-fracture region of the cyclone. The wind acceleration during the descent may involve a combination of frontal dynamics (Schultz and Sienkiewicz, 2013), mesoscale instabilities (Volonté et al., 2018) and evaporative cooling (Eisenstein et al., 2020). The presence of a SJ is often suggested by the banded structure of the cloud head in infrared satellite observations, although a formal identification requires Lagrangian trajectories in numerical simulations (see Clark and Gray, 2018, for a review). Current global models for climate and numerical weather prediction (NWP) are able to represent the WCB, CCB and DI jets (Catto, 2016) but only marginally the SJ, which requires grid spacings under $10\,\mathrm{km}$ in the horizontal and $200\,\mathrm{m}$ in the vertical (Clark and Gray, 2018). Instead, SJ precursors can be identified in global models from diagnostics based on the presence of mesoscale instabilities within the cloud head. Using such a diagnostic, Gray et al. (2024) recently suggested that SJs are potentially ubiquitous in intense cyclones over all oceanic storm tracks albeit do not necessarily result in strong surface winds.

Damages from windstorms are due to surface gusts mostly, which are small-scale and short-lived peak winds measured over 3 s typically (World Meteorological Organization, 2018). The formation of surface winds and gusts associated with mesoscale airflows is not well understood and too small scale to be explicitly represented by current NWP models (Sheridan, 2018). For instance, near-surface winds and gusts are not reliable in reference data sets such as the ERA5 reanalysis (Minola et al., 2020). Different sub-mesoscale processes can be responsible for the downward transport of high momentum from above the boundary layer to the surface. Deep convection has been documented along the cold front, where it can organize into a line that resembles a derecho and results in convective gusts (Ludwig et al., 2014). Boundary-layer structures of high wind have been observed by high-resolution Doppler radar and were associated with evaporating showers below a SJ (Browning et al., 2015). Coherent structures have also been identified below a WCB using a Doppler lidar during a dedicated field campaign (Pantillon et al., 2020).

https://doi.org/10.5194/egusphere-2026-4453
Preprint. Discussion started: 12 August 2026

However, the sub-mesoscale processes leading to surface gusts remain largely unknown. Firstly, their observation relies on rare measurements obtained during the random passage of an extra-tropical cyclone over the ground instrument. Secondly, their accurate modeling requires very fine horizontal grid spacing that is not affordable for operational NWP models. Regional forecasts with $\mathcal{O}(1\,\mathrm{km})$ grid spacing can explicitly represent deep convection but still suffer from large errors in surface gusts during windstorms involving frontal convection (Pantillon et al., 2018). Boundary-layer structures are sub-mesoscale and their explicit representation in windstorms requires even higher resolution of $\mathcal{O}(100\,\mathrm{m})$ (Lfarh et al., 2023; Maury et al., 2026). Thirdly, the downward transport of high momentum is further controlled by environmental conditions that are not fully elucidated. The boundary-layer stability is crucial but also complex, because it differs between the mesoscale airflows and depends on the underlying surface (Hewson and Neu, 2015). For SJs in particular, knowledge about boundary-layer processes is missing and is considered a key limitation (Clark and Gray, 2018).

Over sea, where intense cyclones develop, it has been shown that strong surface fluxes can entrain high-momentum air from a SJ into the boundary layer and to the surface (Schultz and Sienkiewicz, 2013). However, these results were obtained with coarse simulations that do not explicitly represent the processes responsible for downward momentum transport. Furthermore, surface fluxes in windstorm conditions are poorly constrained in models due to the lack of observations for winds above 20–25 $\mathrm{m\,s^{-1}}$ (Edson et al., 2013). For instance, Lfarh et al. (2024) showed how the choice of a parametrization for surface heat fluxes controls the morphology of boundary-layer rolls and the downward transport of momentum in large-eddy simulations (LESs) of a CCB cyclone. Furthermore, the formulation of the drag coefficient is a major source of uncertainty in estimating surface winds in extra-tropical cyclones (Pineau-Guillou et al., 2018) and an accurate representation of the wave-atmosphere interactions can be crucial (Gentile et al., 2021). Efforts are ongoing to better take into account wave impacts on the marine atmospheric boundary layer (MABL) through model coupling (e.g. Pianezze et al., 2018) and updated air-sea flux parameterizations (e.g. Bouin et al., 2024).

Another challenge for modeling windstorms lies is the broad spectrum of scales involved. Extra-tropical cyclones typically extend over $\mathcal{O}(1000\,\mathrm{km})$ and propagate quickly, while the associated winds are transported downward in the boundary layer over scales of $\mathcal{O}(1\,\mathrm{km})$. Realistic LESs (spatial resolution of $\mathcal{O}(100\,\mathrm{m})$) can improve the wind intensity compared to km-scale forecasts (Pantillon et al., 2020). However, they are usually run with small spatial extent and are constrained by the quickly-evolving lateral boundary conditions (Maury et al., 2026). These limitations call for a seamless modeling strategy such as LESs encompassing synoptic-scale systems (Heinze et al., 2017). Building on Lfarh et al. (2023, 2024), this paper follows that seamless strategy and makes extensive use of the Meso-NH atmospheric research model, which contains comprehensive physics packages for a wide range of scales including LESs (Lac et al., 2018). Meso-NH has capability to run over very large grids using demanding physical parameterizations thanks to developments in massively parallel computing (Pantillon et al., 2011) and recent porting to GPU architectures (Escobar et al., 2025). It also includes a surface model that allows coupling with ocean and wave models (Voldoire et al., 2017).

This paper focuses on the winds induced by the extra-tropical cyclone baptized Alex by Météo-France (and Brigitte by the FU-Berlin) that formed over the North Atlantic on September 30th, 2020 (Ginesta et al., 2023). On October 1st, Alex traveled north east across the Bay of Biscay before making landfall over the island Belle-Île and subsequently in the Morbihan, Southern

https://doi.org/10.5194/egusphere-2026-4453
Preprint. Discussion started: 12 August 2026

Brittany, France. Very strong wind gusts were recorded as it made landfall (186 km h^{-1} at Belle-Île and 157 km h^{-1} at the neighboring island of Groix) and weather stations over land recorded 10-min averaged winds of 100 to 130 km h^{-1}. This paper investigates the origin of strong surface winds across scales, from the mesoscale airflows to the sub-mesoscale processes and wave-atmosphere interactions responsible for downward momentum transport. While it is not the focus of the paper, the storm is also known for having generated strong coastal winds along Channel (Maury et al., 2026) on October 2$^{\text{nd}}$ and extreme rainfall in the Mediterranean, particularly in the French department of the Alpes-Maritimes and the neighboring Italian regions of Piemont and Liguria which led to landslides, flooding and over a dozen deaths (Terray and Bador, 2025; Watchers, 2020).

Section 2 describes the model experiments for the atmosphere and wave models, as well as the jet identification. Section 3 first presents an assessment of the numerical simulations, then discusses the impact of resolution and wave coupling, and analyses the jets responsible for extreme surface winds. Section 4 finally delivers conclusions and perspectives of the paper.

2 Methods

2.1 Model Experiments

A series of 9 simulations were run spanning the 6 hours from when Alex entered the Bay of Biscay on October 1 at 18:00 UTC until landfall on October 2 at 00:00 UTC. Each simulation shared the same domain, shown in Fig. 1, with an incremental increase in the horizontal resolution going from a NWP-like grid spacing of 1.6 km to a near-LES grid spacing of 100 m (see Table 1). Five simulations spanning all grid resolutions were atmospheric only. These will be referred to as A*res* where *res* is the horizontal grid spacing in meters. The four other simulations included wave coupling and will be referred to as AW*res*. Due to high computational costs and numerical instabilities, no coupled simulation was run at 100 m resolution.

Table 1. Model Experiments with varying horizontal grids. A and AW refer to atmosphere only and coupled atmosphere-wave, respectively.

Experiment	Horiz. Res.	Grid Size	Meso-NH time step	Configuration
A/AW1600	1600 m	256x256	15 s	NWP-like
A/AW800	800 m	512x512	8 s	LES-like
A/AW400	400 m	1024x1024	4 s	LES-like
A/AW200	200 m	2048x2048	2 s	LES-like
A100	100 m	4096x4096	1 s	LES-like

2.2 Atmospheric model set-up

Model experiments were conducted using the non-hydrostatic atmospheric research model of the French community Meso-NH (Lac et al., 2018) version 5.5.1. The higher resolution runs A800 to A100 were performed using the GPU-ported code including a new pressure solver adapted to hybrid architectures (Escobar et al., 2025). They were all run with the same LES-like physical configuration with fully explicit convection and a 3D turbulence scheme (Cuxart et al., 2000) with a one and a half order closure (i.e. prognostic turbulent kinetic energy (TKE) and diagnostic mixing length). In these simulations the mixing length was given by the mesh size and limited by the ground distance and also by the Deardorff (1980) mixing length in stable cases. For the lower resolution, NWP-like simulation A1600, the subgrid shallow convection eddy-diffusivity-mass-flux scheme (Pergaud et al., 2009) was activated with the 1D version of the turbulence scheme with a mixing length computed according to Bougeault and Lacarrere (1989). No deep convection scheme was activated. For all simulations the vertical resolution was set to 90 levels with a refinement near the surface with a first level at 5 m and a last level at 27.5 km as in the AROME NWP model (Seity et al., 2011). A discretization of fourth order was used for momentum advection and the Piecewise Parabolic method (PPM, Colella and Woodward (1984)) for scalar advection with a Runge-Kutta temporal scheme. The timestep (see Table 1) and the characteristic time (e-folding time) of the fourth order numerical diffusion for momentum were adapted to the horizontal resolution. The single moment ICE3 mixed microphysics scheme (Pinty and Jabouille, 1998) and the radiation scheme of the European Centre for Medium-Range Weather Forecasts (Gregory et al., 2000) were activated. The fast radiative transfer model RTTOV version 13.2 (Saunders et al., 2018) is used to simulate brightness temperatures.

Initial and boundary conditions were given by the operational analysis provided by Meteo-France based on the AROME NWP model (Seity et al., 2011) which was run at 0.01 ° horizontal resolution ($\sim$ 1.3 km) over the French mainland in a grid covering this study's domain. Analysis fields were provided at hourly resolution. They included daily sea surface temperatures from the Copernicus Marine Service Global Ocean OSTIA Sea Surface Temperature and Sea Ice Analysis (Good et al., 2020) at 1/20 ° horizontal resolution ($\sim$ 6 km).

2.3 Representation of air-sea interactions

In Meso-NH, surface fluxes are handled by the externalized surface model SURFEX (Masson et al., 2013) which is common to all French atmosphere models from weather to climate, research to operational. The new Wave-Age Stress dependent Parametrization (WASP, Bouin et al. (2024)) was used over the ocean. WASP was specifically designed to represent wave impacts on momentum fluxes in a coupled model configuration. It allows for variability in the drag coefficient due to wave growth in the 10-m wind speed (U_{10}) range of 7 to 22 $\mathrm{m\,s^{-1}}$ and forces a decrease then saturation of the drag in the higher wind speed range (above 23 and 45 $\mathrm{m\,s^{-1}}$, respectively). Wave growth is taken into account via a wave-age dependent Charnock parameter used to compute the roughness length with the wave age (ω_{ws}) defined in terms of the phase speed of the wind-sea (c_{ws}) as $\omega_{ws} = c_{ws}/U_{10}$. In an atmosphere only set-up, ω_{ws} is assumed constant and equal to 0.5. Wave impacts were thus partially included in the atmosphere-only simulations. In the coupled configuration, a wave model provided a wind-sea period from which the wind-sea phase speed was computed using the linear deep-water wave dispersion relation $c_{ws} = \frac{gT_{ws}}{2\pi}$ where g is the acceleration due to gravity and T_{ws} the mean period of the wind sea. When coupled with a wave model T_{ws} depends on the wave physics and so does the surface roughness, the drag coefficient, and subsequently the surface winds.

2.4 Coupling with a spectral wave model

The third generation wave model WAVEWATCH III ® (WW3; The WAVEWATCH III ® Development Group, 2016), version 7.14, was used in the coupled wave-atmosphere simulations. The horizontal grid of WW3 was set to match that of Meso-NH

https://doi.org/10.5194/egusphere-2026-4453
Preprint. Discussion started: 12 August 2026

but for AW200 where it was run at a lower resolution than the atmosphere on the same grid as AW400. The spectral space was discretized using 36 frequencies ranging from 0.0412 to 1.1573 Hz in 10 % steps (f_{i+1} = 1.1f_i, where i is a discrete grid counter and f the frequency) with 36 directions ($\Delta\Theta$ = 10 °, with a 1st direction set at 5 °). The overall timestep was set to 100 s. The spatial (based on Courant–Friedrichs–Lewy condition without currents) and spectral (refraction) propagation time steps were set to 10 s and 45 s, respectively. The integration of the source function was set to 10 s. The physics package used was “ST4" with original dissipation parameters (Ardhuin et al., 2010). The non-dimensional growth parameter (β_{max}) was set to 1.43, and the short wave sheltering coefficient to 0.3. The TIDE switch was activated allowing for tidal current calculations based on 20 harmonics. The wave model was started from calm conditions (H_s=0 m) and forced at the boundaries by 6 hourly energy spectra extracted from the European Centre for Medium-Range Weather Forecasts (ECMWF) operational analysis on a 0.1 ° × 0.1 ° grid. Meso-NH was coupled to WW3 using OASIS3-MCT (Voldoire et al., 2017). Meso-NH sent WW3 the zonal and meridional 10-m wind components and received from it the peak period of the wind sea partition (T_{ws}) which is used by WASP to compute a wave-age dependent roughness length. Coupling was set to occur every 900 s.

2.5 Identification of mesoscale jets

Lagrangian back trajectories are obtained from passive tracers in Meso-NH (Gheusi and Stein, 2002). The tracers are advected online at every timestep for all model grid points tracking all resolved motion. Back trajectories can then be diagnosed offline given a chosen start and end time. The post-processing generates an output file where for all model grid points at the final time the (x, y, z) position of the back trajectories is saved at a given frequency along with a set of chosen prognostic (e.g., 3D wind components) and diagnostic variables (e.g., relative humidity) interpolated onto that position.

Mesoscale jets linked to the strongest winds (above 35 $\mathrm{m\,s^{-1}}$) at 22:30 UTC were first identified in the NWP-like A1600 simulation based on the Lagrangian back trajectories. Only trajectories in the lower troposphere are considered with the upper limit of 4250 m chosen so as to not include the jet stream. For A1600 trajectories were activated from the start of the simulation and reconstructed from 22:30 UTC back to 18:00 UTC with a 15 minute interval. This mesoscale analysis guided the subsequent identification in the LES-like, atmosphere-only simulations used to study the sub-mesoscale process within the MABL allowing some jets to reach the surface or not. Results on the sub-mesoscale are obtained using A200 for which trajectories were activated only between 21:30 to 22:30 UTC and reconstructed with a 2 minute interval. Computational memory limitation meant no reconstruction was possible for A100 and dictated the highest temporal resolution in A200.

https://doi.org/10.5194/egusphere-2026-4453
Preprint. Discussion started: 12 August 2026

3 Results

3.1 Overall assessment of the simulations

Synoptic cloud features sensed by satellite-borne radiometers are used to provide a global assessment of how closely the simulated storm resembles reality. The simulated cyclone mimics observations well both in terms of scale and position of fronts delimiting cloud cover. This is illustrated in the maps of Fig. 1 (a-f), where Alex is seen approaching the southern Brittany coast of France from the south west. Simulated brightness temperatures (T_B, Fig. 1(d-f)) are compared to the T_B obtained from the MSG SEVIRI satellite (Fig. 1(a-c)). While only results of A1600 are shown in Fig. 1(d-f), all simulations are comparable in the aforementioned aspects. The simulated storm is slightly delayed and further to the south west than Alex was at landfall. Dry bands are visible in the remotely sensed T_B on the outer edge of the cloud head. The tip of cloud head also appears to split into two in the satellite imagery (Fig. 1(a-c)). These are considered indices for sting jets (Clark and Gray, 2018). Banding within outer (southern) edge of the cloud head is well reproduced by Meso-NH already at 1.6 km resolution (not shown). While cloud head splitting is reproduced in the simulated T_B, arc shaped features are visible in the leading edge of the cloud head (Fig. 1(d-f)).

The MetOP-A satellite passed over Alex on October 1st around 20:27 UTC providing ocean surface wind vectors from the Advanced Scatterometer (ASCAT) at 12.5 km sampling (25 km effective) resolution. These are shown in Fig. 1(a). The high wind core is located south east of the cloud head with maximum winds around 25.8 $\mathrm{m\,s^{-1}}$, which is consistent with the expected location of a sting jet. The simulated winds over the ocean are comparable to those provided by ASCAT at 20:30 UTC (Fig. 1(a and d)). The location of the simulated high wind core is also slightly shifted with respect to that of the cloud head: it is more its interior/northern side rather than directly at its tip as seen in satellite observations.

The simulated horizontal wind field at 500 m altitude (Fig. 1(g-i)) displays two regions of enhanced winds : 1) a main core, where the strongest winds are simulated, which turns cyclonically around the center from the north west to the south and corresponds to the leading edge of the bent back front and 2) a larger band roughly oriented south-north associated with the warm conveyor belt ahead of the cold front. The strongest winds within the main wind core are situated towards the interior or northern side of the bent back front. They increase as Alex approaches the coast. The focus of subsequent analysis will be on the jets leading to the maximum winds during landfall at 22:30 UTC within the main wind core highlighted by the cyan box in Fig. 1(i).

Very few in situ data are available over the ocean to validate surface atmospheric parameters. In particular, no meteorological buoy is situated within the model domain. The simulated 10-m winds and mean sea level pressures (MSLP) are thus validated against measurements of the Météo-France weather station network. Timeseries of the measured and simulated surface variables are shown in Fig. 1(j,k) for four coastal stations whose locations are marked in Fig. 1(c). Wind speed measurements (Fig. 1j) are given at 6 minute (black lines) and hourly interval (black symbols) on all four stations. They are seen to ramp up after 19:00 UTC with strongest winds of 30.2 $\mathrm{m\,s^{-1}}$ recorded at Belle-Île at 22:00 UTC (stars). Note that infra-hourly measurements are not available around the time the strongest winds were recorded on Belle-Île. Also, the wind record on the island of Groix shows erroneously low values around the time the strongest winds hit it (squares). Nevertheless, all the station hint to maximum winds between 21:30 UTC and 22:30 UTC. The 10-m wind speeds in the A200 simulation within a radius of $2\,\mathrm{km}$ of the stations (red shading) start ramping up around 20:00 UTC and the peak on Belle-Île occurs around 22:30 UTC, when it reached $30.7\,\mathrm{m\,s^{-1}}$, which matches observations well in terms of magnitude. There is thus a 30 minute to one hour delay in the storm's arrival in the simulation compared to measurements, consistent with the delay in T_B. In general the simulated wind speeds are lower by several $\mathrm{m\,s^{-1}}$ than the measured ones even when accounting for the time-shift. Only the station on Belle-Île is equipped with a pressure sensor providing hourly records, which recorded a minimum MSLP at 22:00 UTC of $974.3\,\mathrm{hPa}$ (black line in Fig. 1k). The simulated MSLP on Belle-Île shows a 30 minutes to 1 hour delay compared to the measurements, also consistent with the delay in T_B, with a deeper minimum around 22:30 UTC of $972.2\,\mathrm{hPa}$ (red stars). That simulated around the island of Groix, north of Belle-Île, closely follows observations at Belle-Île, matching the minimum at 22:00 UTC (red squares).

Overall, this analysis gives confidence in the realism of the simulation. It confirms their adequation to the study the origins of surface wind extremes from the meso to the sub-mesoscale after an assessment of the impacts of resolution and wave coupling on surface winds.

3.2 Impacts of resolution and wave coupling

The impacts of resolution and wave coupling are illustrated in Fig. 2 in terms of changes in the magnitude of the top $2\,\%$ strongest 10-m wind speeds over the ocean. In the LES-like simulations, A800 to A100, the higher the resolution the lower the winds during the first hours (Fig. 2). During peak intensity (21:00-22:30 UTC), values of wind extremes converge for horizontal grid spacing of $400\,\mathrm{m}$ and lower. Wind extremes of the NWP-like A1600 simulation start off higher than those in A200 and A100 until 20:00 UTC at which point convergence is observed. During peak intensity, wind extremes in A1600 are slightly weaker than those of the LES-like simulations. The simulations A(W)800 appear as outliers with higher extreme winds than all other simulations. This can be attributed to the lack of shallow convection scheme which results in a less mixed/less stable marine boundary layer. Given the convergence of wind extreme values in LES-like simulations starting at 400 m resolution and closeness of wind extremes in A1600 and A200 further analysis will focus on these two simulations. Waves impacts are discussed in the rest of this section but not taken into account for the analysis pertaining to the origins of the high surface wind speeds.

Wave coupling leads to a reduction in the surface winds of about $1\,\mathrm{m\,s^{-1}}$ across all resolutions, particularly as the winds ramp up (18:00-22:00 UTC) and are over $18\,\mathrm{m\,s^{-1}}$ (Fig. 2b). The wind sea is generated and grows as the wind ramps up, thus wave coupling leads to an increased roughness which accounts for the reduction in surface wind extremes. Figure 3 shows the regions in which the wind-sea wave age ω_{ws} is over (under) estimated in orange (purple) in the atmosphere only simulation A200 compared to the corresponding coupled wave-atmosphere simulation AW200 at 20:30 UTC when Alex is still mostly over the ocean. Surface wind contours demark regions where it exceeds $22\,\mathrm{m\,s^{-1}}$ in A200 allowing to localize the high wind core and the larger band ahead of the cold front. There is a clear geographic distinction between regions where 1) the wind-sea is younger in AW200 than in A200 (ω_{ws} < 0.5, orange) ahead of the cold front, north, and east of the low pressure system and 2) the wind-sea is older (ω_{ws} > 0.5, purple) behind the cold front and generally to the west and south of the low pressure

https://doi.org/10.5194/egusphere-2026-4453
Preprint. Discussion started: 12 August 2026

center with the exception of the high wind core on the leading edge of the bent back front. Within the high wind core, lack of coupling leads to a wind-sea wave age overestimation in the leading region (ω_{ws} < 0.5 in the red square labeled B in Fig. 3) where the winds are the strongest (cf. Fig. 1(g)) and an underestimation in the rear (ω_{ws} > 0.5).

In order to illustrate the atmospheric response to these wave age biases, power density distributions of the drag coefficient and of the 10-m winds were computed from A200 and AW200 in three equal sized boxes: on either side of Alex's center (blue and orange squares labeled A and C, respectively, in Fig. 3) with similar median wind speeds ($\sim 17.5\,\mathrm{m\,s^{-1}}$) as well as within the high wind core (red square B). These are shown in Fig. 4. A contrasted response to coupling becomes apparent when comparing A200 (cyan) with AW200 (purple): 1) where $\omega_{ws} < 0.5$ ahead of the cyclone, there is a clear shift in the distributions with an increase in the drag coefficient C_D (Fig. 4c) and a resulting reduction in U_{10} with less winds over $18\,\mathrm{m\,s^{-1}}$ (Fig. 4f), and 2) where $\omega_{ws} > 0.5$ behind the cyclone, the drag response is more complex with a widening of the distribution (Fig. 4a) and a narrowing of the U_{10} distribution around $17\,\mathrm{m\,s^{-1}}$ (Fig. 4d). Within the high wind core (box B, Fig. 4b,e) the impacts of waves is a mixture of that seen in regions A and C. The drag coefficient increases over much of the high wind core but unlike in box C there is no significant increase of the maximum values of the distribution. The wind speed distribution is bimodal in both A200 and AW200 as some lower wind grid points around the main wind core are included. The wave induced decrease in 10-m wind speeds is limited to the range of 20-25 $\mathrm{m\,s^{-1}}$ similar to what is observed in box C, while a decrease is seen in the range of 14-20 $\mathrm{m\,s^{-1}}$, similar to what is observed for box A. Observed changes in drag coefficient and wind speed arise by design of WASP (see section 2.3).

3.3 Jets responsible for extreme surface winds

Mesoscale jets associated with horizontal wind speeds exceeding $35\,\mathrm{m\,s^{-1}}$ at 22:30 UTC within the high wind core (region of interest delimited by the square in Fig. 1(i)) in the lower troposphere (< 4250 m) were classed into four jets according to altitude and relative humidity following the conceptual model of mesocale jets as summarized in the flowchart in Fig. 5. Trajectories were separated as follows: 1) those which remain throughout the Lagrangian reconstruction in the lower 2500 m corresponding to the Cold Jet (CJ, in green), 2) the remaining whose relative humidity was inferior or equal to 80 % at a given time (t_{RH}, defined below) corresponding to the Dry Intrusion Jet (DJ, in purple), 3) the remaining which plunge by more than 1.5 km within the last hour of the Lagrangian reconstruction corresponding to a Sting Jet (SJ in pink), and 4) the remaining that are attributed to a potential Sting Jet (PotSJ, in turquoise), as discussed below. The order of application of these criteria allows unique attribution of jet labels to each trajectory.

The same criteria were applied to both A1600 and A200 with the only difference being the time of application of the first two criteria on account of different start and thus duration of Lagrangian reconstruction. The first criterion, on altitude, was based on visual inspection of the time variation of altitudes of all trajectories in A1600 where a separation around 2500 m was visible at the beginning of the simulation when the DJ is presumed to be absent of the lower troposphere. It aligns with the conceptual idea that the cyclonic branch of the CCB remains confined in the lower 700 hPa (Schultz, 2001; Martínez-Alvarado et al., 2018). The second criterion, on humidity, was determined by trial and error. In A1600, applying the humidity criteria to the initial 2 hours of the Lagrangian reconstruction gave the most coherent grouping based on visual inspection of main jet

https://doi.org/10.5194/egusphere-2026-4453
Preprint. Discussion started: 12 August 2026

properties and origins. The third criteria was chosen such that it could be applied equally to A1600 and A200 and implies that the trajectories associated to the SJ were at an altitude of over 1.5 km above the surface at 21:30 UTC. This altitude was chosen somewhat arbitrarily to be above the median altitude of the CJ and around the height of the cloud base.

The time evolutions of main properties of the four jets diagnosed in A1600, with t_{RH} spanning 18:00 to 20:00 UTC, are illustrated in Fig. 6. The CJ trajectories (green lines) have a median altitude of 1.1 km throughout the trajectories' reconstruction with the 75$^{\text{th}}$ percentile not exceeding 1.8 km (Fig. 6a). They remain very humid throughout the reconstruction with a median $RH > 93\,\%$ (Fig. 6(b)). The wind speed of all jets is seen to accelerate after 20:30 UTC (Fig. 6c). The final median wind speed of the CJ is the strongest of all jets reaching 39.8 $\mathrm{m\,s^{-1}}$ with a 75$^{\text{th}}$ percentile of 44.2 $\mathrm{m\,s^{-1}}$.

The SJ (pink lines) originates from within the CCB height range with median initial altitudes of 1.2 km. It ascends to 3.9 km between 19:00 and 20:45 UTC after which point it descends to return to a median altitude of 1.1 km at 22:30 UTC. Relatively constant RH over 95 % can be observed for the SJ within the first half of the Lagrangian reconstruction. The SJ is seen to dry after 21:30 UTC as it descends, reaching a median value of ∼80 % at 22:30 UTC. Acceleration of the winds within the SJ starts around 20:30 UTC which roughly corresponds to the onset of its descent. The initial median wind speed of the SJ is the higher that that of the CJ (17.4 vs. 13.6 $\mathrm{m\,s^{-1}}$). The final median wind speed of the SJ is barely lower than that of the CJ with value of 39.6 $\mathrm{m\,s^{-1}}$ and its 75$^{\text{th}}$ percentile is also slightly lower reaching 43 $\mathrm{m\,s^{-1}}$. The altitude evolution of the SJ and its humid character match the definition put forward by Clark et al. (2005) and Clark and Gray (2018) as a jet descending from the cloud head. The altitude evolution though comparable to that documented for other storms through modeling studies (e.g., Volonté et al., 2024a, b; Gray and Volonté, 2024; Suri et al., 2025), occurs over shorter timescales. For instance, the SJ identified during storm Ciarán by Volonté et al. (2025) is seen to rise and subsequently subside over a period of more than 7 hours versus less than 4 hours here. Observed drying during descent suggests evaporative cooling of the SJ which has been put forward as a mechanism promoting its descent as it leaves the cloud head (Clark et al., 2005; Clark and Gray, 2018).

As expected, the DJ (purple lines) originates from the mid-troposphere and is seen to gradually descend to reach a median altitude of 1.8 km at the end of the reconstruction. Note that because a majority of DJ trajectories originate from outside of the model domain, their characteristics are only considered starting at 19:15 UTC. The classical criterion used for a Lagrangian diagnosis of DI is a minimum descent of about 400 hPa during 48 hours (Raveh-Rubin, 2017). The observed descending rate of the DJ (> 3 km in 3 hours) thus largely satisfies this criterion albeit applied to a much shorter period. After 21:30 UTC, the altitudes of the SJ and DJ are indistinguishable, thus confirming the necessity of a relative humidity criterion to distinguish them. The very dry character of the DJ stands out clearly between 19:15 and 21:00 UTC with a median RH of 28 %. As the DJ descends its relative humidity increases before plateauing around 22:00 UTC around a median value of 77.5 %. Drying of the SJ and humidification of the DJ makes them barely distinguishable using a RH criterion the closer they get to the surface. The initial wind speed of the DJ exceeds that of the other jets following the expectation of higher momentum being found at higher altitudes. The DJ's winds remain relatively constant around 21 $\mathrm{m\,s^{-1}}$ until 21:00 UTC after which they increase more gradually than that of other jets reaching at 22:30 UTC a median value of 38.1 $\mathrm{m\,s^{-1}}$ with a 75$^{\text{th}}$ percentile of 41.3 $\mathrm{m\,s^{-1}}$.

The PotSJ (turquoise lines) was labeled as such because of its origins and altitude evolution mimic that of the SJ. Starting at median altitude of 1.1 km, it ascend to 2.6 km between 19:00 and 21:00 UTC. It remains around this median level until

https://doi.org/10.5194/egusphere-2026-4453
Preprint. Discussion started: 12 August 2026

the end of the reconstruction which does not allow confirming whether it eventually descends like the SJ. The PotSJ remains very humid ($RH > 91\,\%$) throughout the reconstruction. Its winds are seen to accelerate from a median value of $15.5\,\mathrm{m\,s^{-1}}$ at 18:00 UTC to $38.7\,\mathrm{m\,s^{-1}}$.

Figure 6(d) shows the trajectories color-coded by group in a storm-centric projection around the minimum MSLP location. It confirms the categorization of trajectories following the classical conceptual model of an extra-tropical cyclone in the northern hemisphere with 1) the CJ (green) trajectories originating east of the cyclone center and wrapping around it anti-clockwise, 2) the DJ (purple) originating outside of the system on the north-west and wrapping around the cyclone center as it descends, 3) the SJ (pink) and 4) the PotSJ (turquoise) whose trajectories follow those of the CJ. While not visible in Fig. 6(d), a small number of trajectories identified as belonging to the DJ originate from within the CJ and SJ region. This likely misidentification can be due to the relatively simple criteria chosen to distinguish jets. The median position of the DJ (square) and SJ (dots) and associated time stamps reveal that both join each other and become undistinguishable shortly after 21:30 UTC on the west side of the cyclone center. A progressive acceleration of the winds is to be expected also when the jets start aligning with the cyclone's propagation direction (west-east in the storm-centric view). Starting around 21:00 UTC jets no longer travel opposite to the cyclone's propagation (Fig. 6c) which likely contributes to the observed acceleration of jet winds.

3.4 Robustness of the jet identification across spatio-temporal resolutions

Since one of the goals of this study is to investigate fine-scale circulations allowing jets to reach the MABL, the next section focuses on the LES-like run A200 as such circulations are not resolved in the NWP-like run A1600. However, in A200 trajectories were reconstructed only during the last hour of the descent of the SJ and DJ, i. e., from 21:30 to 22:30 UTC. Thus the t_{RH} best fitted to A1600 cannot be applied to A200. Instead, for the analysis of A200, t_{RH} was set to 21:30 UTC which is the earliest possible time. The reduced time-frame over which the trajectories were computed in A200 and the different t_{RH} induces jet identification mismatches between the classification in A1600 illustrated in section 3.3 and A200 used in section 3.4. Mismatches are determined in A1600 by comparing labels associated to trajectories when considering 1) the whole Lagrangian reconstruction with t_{RH} spanning 18:00 - 20:00 UTC , and 2) considering the Lagrangian reconstruction only between 21:30 and 22:30 UTC and setting t_{RH} to 21:30 UTC. Results are illustrated in terms of vertical profiles of number of trajectories in each of the 4 jets and their proportions at 22:30 UTC. Changes in time-frame considered in A1600 full (solid lines) vs reduced (dashed lines) are shown in Fig. 7(a and b)). Comparing these profiles to those obtained with A200 Fig. 7(c and d) can reveal additional changes due to resolution.

Some aspects of the vertical distributions of jets are independent of the considered time-frame and are similar for both A1600 and A200. The total number of high wind trajectories (black lines) increases sharply with height up to $1\,\mathrm{km}$, from which point it decreases slightly. A second peak in number of high wind trajectories is seen around $3\,\mathrm{km}$ altitude above which it decreases sharply. The CJ (green) is responsible for the majority of high winds at low levels up to an altitude of $2\,\mathrm{km}$. By construct the number of CJ trajectories (green) goes to zero at an altitude of $2.5\,\mathrm{km}$. Consequently the number of PotSJ (turquoise) are seen to increase as the number of CJ trajectories decreases. The PotSJ trajectories are concentrated at a height of about $2.5\,\mathrm{km}$ where they make up $75\,\%$ of the high wind trajectories. The number of SJ (pink) and DJ (purple) trajectories start becoming

https://doi.org/10.5194/egusphere-2026-4453
Preprint. Discussion started: 12 August 2026

important above 200 m with a maximum around 250 m and 500 m for the DJ and SJ respectively. Unlike the other three jets, whose vertical distributions are largely uni-modal, the DJ is found in high concentration centered around two different altitudes (∼1.2 km and ∼3.2 km).

Reducing the time-frame over which jets are classed in A1600 leads to around 20 % of trajectories originally classed as DJ, SJ, and PotSJ to be identified as CJ (compare dashed with solid curves in Fig. 7a,b). These correspond to trajectories which had already subsided below 2.5 km by 21:30 UTC. The over attribution to CJ trajectories is not substantial in the lower 500 m. Indeed, the difference between the solid and dashed profiles for the CJ is around 25 % above 1 km but around 5 % or less below 500 m. Setting the time when the RH threshold is applied to 21:30 UTC leads to 6.6 % of DJ to be identified as SJ and 4.6 % as PotSJ. Inversely, 7.3 % SJ and 10.5 % PotSJ becomes DJ. Note that the number of trajectories identified as SJ does not change substantially at any altitude when shortening the time considered for the trajectories' reconstruction.

Vertical distribution of jets in A200 generally matches results obtained with A1600, particularly those over the reduced time frame with a potential over attribution of CJ trajectories above 500 m altitude. Differences between the A1600 reduced time-frame analysis and A200 are noticeable only for the DJ (compare dashed curves in panels a, b with panels c, d). The proportion of DJ trajectories in A200 is slightly reduced in the lower troposphere but increased above 3 km. This analysis thus suggests that mismatches are not substantial in the lower troposphere giving confidence in the use of the trajectory reconstruction in A200 over the reduced time-frame to further investigate small scale circulations. In A200, within the lower 500 m the CJ is responsible for the majority of the strong winds, making up 91 % of the high wind trajectories while the SJ and DJ make up 6 % and 3 %. The CJ also has the highest wind speed within the lower 500 m with a median value of 39.5 $\mathrm{m\,s^{-1}}$ and a 98$^{\text{th}}$ percentile of 51.4 $\mathrm{m\,s^{-1}}$, while for the SJ, the median wind speed is 39.1 $\mathrm{m\,s^{-1}}$ and the 98$^{\text{th}}$ percentile is 49.6 $\mathrm{m\,s^{-1}}$ and for the DJ, the median is 38.5 $\mathrm{m\,s^{-1}}$ and the 98$^{\text{th}}$ percentile is 46.8 $\mathrm{m\,s^{-1}}$.

3.5 Role of sub-mesoscale coherent structures

The final location of jets making up the high wind core diagnosed in A200 are shown in maps and vertical cross-sections along (P1–P2, Fig. 8) and across wind (P3–P4, Fig. 9). The maps in Fig. 8(a) and (c) show that the SJ (pink dots) and DJ (purple dots) that reach the lower 1000 m are located in the south-western (outer-rear) part of the high wind core with the DJ occupying the outermost parts. Three regions of high winds (shading in Fig. 8(b)) descending from the mid troposphere are discernible at the rear of P1–P2. The outer one corresponds to the outer edge of the cloud head discernible in Fig. 8(d) as the high RH feature descending from the mid-troposphere at P1. The cloud head is flanked by dry regions. Two are visible in the cross section: one reaching the surface along its outer edge and one above 3000 m. High winds are located at both edges of the cloud head and the dry side is where the DJ trajectories are found. There are thus two geographically distinct DJs: a surface one in the rear (west) of the high wind core and an upper one located further east. The lower DJ appears embedded within the SJ. The PotSJ (turquoise dots) makes up the high winds within the cloud head above 2 km. Some SJ and PotSJ trajectories are found scattered throughout the CJ (green dots). A small group of trajectories identified as SJ is found at boundary between the PotSJ and the upper DJ branch, highlighting a region of enhanced subsidence. These should likely be associated to DJ based on the previously described analysis on jet association mismatch due to the shortened trajectory reconstruction time.

https://doi.org/10.5194/egusphere-2026-4453
Preprint. Discussion started: 12 August 2026

Few SJ trajectories and no DJ trajectories are found within the MABL whose height (orange line) was estimated based on the critical value of 0.25 of the gradient Richardson number. Within the high wind core, the MABL is thinnest in the region of SJ and DJ descent (km 25-40 of the cross section P1–P2), with heights under 200 m. Its height gradually increases to around 500 m halfway through the high wind core and fluctuates around that level further east. The CJ is found consistently within the MABL at the center of the high wind core (km 40-80 of P1–P2). Towards the outer forward edge of the high wind core (km 80-130 of P1–P2), the CJ is present only intermittently and appears to be brought to the surface at somewhat regular intervals of $\sim$ 5 km between km 100 and 120. In this region, banding (succession of high and low or positive and negative values) is visible in the horizontal velocity (Fig. 9 (a)), the vertical velocity (Fig. 9 (c)) and the evaporation (Fig. 9 (e)). Vertical velocities in the lower km of the troposphere (Fig. 9 (c)) are mostly negative in the south western side of the high wind core where the SJ and DJ descend. Along the outer edge of the high wind core is a band of strong ascending motion. Outwards from this band of positive vertical velocities are successive bands of up and down drafts.

To illustrate the coherent structures responsible for the banding and the downward transport of high momentum air masses, a second vertical cross section intersecting the bands, P3–P4, is shown in Fig. 9 (b), (d), and (f). On the inner, northern side and at the center of the high wind core (km 0 to 15 in P3–P4), the CJ (green dots) occupies the MABL and the lower troposphere (up to $\sim$ 2.5 km by construction). In that region the PotSJ (turquoise dots) is confined above the CJ. On the outer, southern side of the high wind core (beyond km 15 in P3–P4), the CJ mostly resides above 500 m, i.e., beyond the MABL, and is brought down at somewhat regular intervals (Fig. 9(b)). Regions where the high momentum air masses reach the surface correspond to regions of downdrafts with negative vertical velocities within the lower 2 km (blue shading in Fig. 9(d)). The sequence of down and up drafts repeats itself several times after km 20 in P3–P4 with each ascending or descending branch measuring between 1 and 2.5 km horizontally. There is a clear correspondence between the MABL height and the branches of the coherent structures. As expected, the MABL is higher under the updrafts and lower in the downdrafts.

The innermost downdraft is the strongest and largest in both horizontal and vertical extents, with negative vertical velocities exceeding -2 m s^{-1} between 250 m and 3 km altitude. This downdraft brings the PotSJ towards the surface. The few trajectories identified as SJ (pink dots) around km 25 at the lower tip of the PotSJ intrusion stem from the same jet as the PotSJ but subsided at a faster rate. The innermost downdraft is located at the southern edge of a mixed phased cloud as indicated by the presence of cloud ice and water in Fig. 9(d) (yellow and black contours). Under the cloud and in particular within the region of PotSJ subsidence there is rain (yellow contours in Fig. 9(f)) with a hotspot of evaporation (shading). This is indicative of evaporative cooling as a mechanism brought forward for SJ subsidence. Smaller mixed phase clouds are also seen over the subsequent downdrafts (Fig. 9(d)). However rain and associated evaporation are only significant within the innermost downdraft (Fig. 9(f)). Nevertheless, trajectories identified as PotSJ and SJ are present within the downdraft around km 28 of P3–P4. While strong rain and evaporation are also present on the inner, northern, side of the high wind core (km 10 to 18 along P3–P4), they are not associated with strong subsidence. The vertical velocity (Fig. 9(d)) shows that in that region vertical motion is confined within shallower layers and there is no continuous up or downdraft throughout the lower 2 km which would allow subsidence of the PotSJ.

https://doi.org/10.5194/egusphere-2026-4453
Preprint. Discussion started: 12 August 2026

4 Conclusions

The explosive extra-tropical storm Alex was studied through a series of NWP- and LES-like Meso-NH atmospheric simulations with and without wave coupling, with horizontal grid spacing halving from 1.6 km to 100 m over a common domain covering the Bay of Biscay and the west coast of France. Simulations were first assessed against available satellite observations (MSG for clouds, ASCAT for winds) and coastal weather station data. These confirmed the model's ability to correctly represent the synoptic situation and location of the high surface wind despite some delay and southward shift. Next, the dependence of simulated surface wind extremes on horizontal model resolution and wave coupling were evaluated. The 98$^{\text{th}}$ percentile of the 10-m winds of all atmosphere-only simulation converge at the time of peak intensity for grid spacing of 400 m and finer. It is reduced by wave coupling by 0.5 to 1.5 $\mathrm{m\,s^{-1}}$ throughout the course of the simulations with little dependence on resolution. Storm relative impacts of wave coupling were then illustrated with contrasting effects on surface winds, with winds mostly decreasing ahead of the cold front (warm conveyor belt jet) and within the high wind core in the frontal fracture region due to wave generation while increasing elsewhere.

Convergence of wind extremes and close match in synoptic evolution gave confidence in being able to focus subsequent analysis on the NWP-like simulation at 1.6 km resolution and the LES-like simulation at 200 m resolution. The origins of high winds in the lower troposphere (up to 4.25 km) within the frontal fracture region just prior to Alex's landfall in Brittany were investigated through online Lagrangian trajectories in these two simulations. Through a series of altitude and humidity criteria, trajectories were associated with mesoscale jets revealing four types of jets at play. The Cold Jet, associated with the cold conveyor belt, is responsible for about 50 % of the high wind trajectories (U>35 $\mathrm{m\,s^{-1}}$) in the lower troposphere. Within the bottom 500 m, the Cold Jet accounts for 91 % of the high wind trajectories and is responsible for the highest wind speeds. A Sting Jet with an embedded Dry Jet is found in the lower 0.2 to 2 km at the rear-outer part of the high wind core. The Sting Jet makes up only 6 % of the high wind trajectories within the bottom 500 m with median winds comparable to those of the Cold Jet but lower extremes. The Dry Jet brings mostly weaker winds than the Cold Jet and Sting Jet, making up only 3 % of the high wind trajectories under 500 m altitude. A fourth jet is detected above the Cold Jet within the cloud head. It is shown to have risen from the lower troposphere like the sting jet but at a later time. It has not yet subsided during the Lagrangian analysis and is thus called Potential Sting Jet. A second, branch of the Dry Jet is found above the Potential Sting Jet. Sub-mesoscale coherent structures consisting of successive up and down drafts are shown to locally bring the Potential Sting Jet towards the surface. These are located at the outer-forward edge of the cloud head spanning over 10 km in length over a width of several kilometers and a height of $\sim$2 km. Jet subsidence is associated with precipitating mixed phase clouds and elevated rain evaporation rate hinting to moist-diabatic processes at play.

Overall this study sheds some insights in sources of high winds at unprecedented high horizontal resolution. Identification of high wind jets through analysis of Lagrangian trajectories is shown to be possible using simple humidity and altitude criteria over a six hour period. Jets are harder to distinguish over shorter periods over which high resolution trajectories are feasible. Dependence of results on time-frame and criteria applied can complicate comparison and application to other case studies. A systematic analysis across model resolution with an assessment of sensitivity of classification criteria used is necessary.

https://doi.org/10.5194/egusphere-2026-4453
Preprint. Discussion started: 12 August 2026

Results match the mesoscale conceptual model of jets in extra-tropical cyclones (Carlson, 1980; Browning, 2004). The Sting Jet evolves as expected, rising from the lower to the mid troposphere before subsiding and exiting the cloud head. However, its location is unlike that of previously studied sting jets (e.g. Rivière et al., 2020; Volonté et al., 2024a; Clark and Gray, 2018) which are typically found on the leading edge of the high wind core ahead of the Cold Jet and not behind as found here. What is more, at the time analyzed here, boundary-layer rolls do not appear to play a key role in bringing down high momentum air unlike high-resolution numerical simulations of Storm Alex at a later time (Maury et al., 2026) and in the cloud head of other intense storms (e.g. Lfarh et al., 2023; Rivière et al., 2020). Coherent structures which bring down high winds from the lower troposphere differ in both location and size from the convective roll vortices described by Rivière et al. (2020) in their idealized numerical simulations of a Sting Jet extra-tropical cyclone. They are larger, extending over 2 km in altitude and located parallel to the southern (outer) flank of the high wind core rather than at its forward edge. Largest jet subsidence is observed in the innermost downdraft associated with these coherent structures.

To assess the veracity of these model efforts measurements are key. It is necessary to go beyond the available meteorological in situ measurements which are largely missing over the ocean. Coordinated international efforts for field campaigns concentrating research instrumentation are essential. While ground-based measurements can provide the necessary temporal resolution, provided they are by chance on the path of an extra-tropical cyclone, air-borne measurements can more easily sample the frontal fracture regions where the high winds are expected albeit for a short time scale. The NAWDIC-DICHOTOMI (Quinting et al., 2026; Rivière et al., 2026) field program including both ground-based and air-borne deployments represents the latest such effort. It will allow shedding light into fine scale characteristics of high wind regions in extra-tropical cyclones. Humidity and 3D wind vertical profiling, as possible using LiDAR and RaDAR, provide the bare necessary measurements to reproduce the jet identification as done here. Cloud micro-physics and turbulence measurements further allow elucidating processes at play. Continuous efforts should also be made in bringing together the air-sea and storm communities to augment marine boundary layer sampling using ships such as during HiWinGS (Blomquist et al., 2017), buoys that weather hurricanes (Potter et al., 2015), and drones (Foltz et al., 2026; Zappa et al., 2020). These would greatly contribute to further investigation of the role of boundary layer processes, air-sea interactions, and waves in near surface wind extremes.

Code and data availability. The simulations were run with open source community codes. Meso-NH is freely available under CeCILL-C license agreement on https://src.koda.cnrs.fr/mesonh/mesonh-code and WAVEWATCH III® is available on https://github.com/NOAA-EMC/WW3. The model data are archived in the GENCI computing center where they were run. The whole data set exceeds 10 Terabytes but subsets can be provided on request to the authors. The MetOp-A ASCAT Level 2 Coastal Ocean Surface Wind Vector Product was retrieved from https://user.eumetsat.int/. French weather station data are available on https://donneespubliques.meteofrance.fr/.

Video supplement. The following video shows output of the simulation made with the atmospheric model Meso-NH with a horizontal resolution of 100 m during a GENCI-CINES "Grand Challenge" pilot project on the Adastra GPU supercomputer. In it the extra-tropical cyclone Alex is seen crossing the Bay of Biscay on October 1 starting at 18:00 UTC and making landfall on the French coast in Brittany

https://doi.org/10.5194/egusphere-2026-4453
Preprint. Discussion started: 12 August 2026

on October 2 at 00:00 UTC. Shown in grey shading are the clouds, with regions of high 10-m winds ($\geq 100\,\mathrm{km\,h^{-1}}$) and extreme rain ($\geq 20\,\mathrm{mm\,h^{-1}}$) overlay in red and blue, respectively.

Author contributions. SEB performed the trajectory experiments, the analysis, wrote, and created the visualizations for this article. FP was responsible for the initial conceptualization, funding acquisition, and coordination of the research project on how wind gust reach the surface. FP also performed the initial model experiments on this case study. JP performed all model simulations, including their implementation and execution on Adastra's CPU/GPU architecture. The methodology was developed by FP and SEB. NM sought and prepared the data and analysis for assessing the realism of the simulations. All co-authors participated in discussions leading to the finalization of this work.

Competing interests. FP is a member of the editorial board of Weather and Climate Dynamics.

Acknowledgements. This work was funded by the French National Research Agency (Grant ANR-21-CE01-0002) and performed using HPC resources from GENCI-CINES (Grants gda2203 and lat0569 A0160111437). SEB benefited from a STSM Grant from the COST Action CA19109 which funded scientific visit to the Department of Meteorology at the University of Reading. We thank the colleagues there for their discussion around the preliminary work that led to this publication. We acknowledge the French National Research Infrastructure CLIMERI-France https://climeri-france.fr/ which provides national label for the code Meso-NH.

https://doi.org/10.5194/egusphere-2026-4453
Preprint. Discussion started: 12 August 2026

References

Ardhuin, F., Devaux, E., and Pineau-Guillou, L.: Observation et prévision des seiches sur la côte Atlantique française, in: Actes des Xèmes journées Génie côtier-Génie civil, Les Sables d'Olonne, pp. 87–94, Centre Français du Littoral, https://doi.org/DOI:10.5150/jngcgc.2010.001-A, 2010.

Bentley, A. M., Bosart, L. F., and Keyser, D.: A Climatology of Extratropical Cyclones Leading to Extreme Weather Events over Central and Eastern North America, Monthly Weather Review, 147, 1471–1490, https://doi.org/10.1175/MWR-D-18-0453.1, publisher: American Meteorological Society Section: Monthly Weather Review, 2019.

Blomquist, B. W., Brumer, S. E., Fairall, C. W., Huebert, B. J., Zappa, C. J., Brooks, I. M., Yang, M., Bariteau, L., Prytherch, J., Hare, J. E., Czerski, H., Matei, A., and Pascal, R. W.: Wind Speed and Sea State Dependencies of Air-Sea Gas Transfer: Results From the High Wind Speed Gas Exchange Study (HiWinGS), Journal of Geophysical Research: Oceans, 122, 8034–8062, https://doi.org/10.1002/2017JC013181, 2017.

Bougeault, P. and Lacarrere, P.: Parameterization of Orography-Induced Turbulence in a Mesobeta-Scale Model, Monthly Weather Review, 117, 1872–1890, https://doi.org/10.1175/1520-0493(1989)117<1872:POOITI>2.0.CO;2, 1989.

Bouin, M.-N., Lebeaupin Brossier, C., Malardel, S., Voldoire, A., and Sauvage, C.: The wave-age-dependent stress parameterisation (WASP) for momentum and heat turbulent fluxes at sea in SURFEX v8.1, Geoscientific Model Development, 17, 117–141, https://doi.org/10.5194/gmd-17-117-2024, 2024.

Browning, K. A.: The sting at the end of the tail: Damaging winds associated with extratropical cyclones, Quarterly Journal of the Royal Meteorological Society, 130, 375–399, https://doi.org/10.1256/qj.02.143, 2004.

Browning, K. A., Smart, D. J., Clark, M. R., and Illingworth, A. J.: The role of evaporating showers in the transfer of sting-jet momentum to the surface, Quarterly Journal of the Royal Meteorological Society, 141, 2956–2971, https://doi.org/https://doi.org/10.1002/qj.2581, 2015.

Carlson, T. N.: Airflow Through Midlatitude Cyclones and the Comma Cloud Pattern, Monthly Weather Review, 108, 1498–1509, https://doi.org/10.1175/1520-0493(1980)108<1498:ATMCAT>2.0.CO;2, 1980.

Catto, J. L.: Extratropical cyclone classification and its use in climate studies, Reviews of Geophysics, 54, 486–520, https://doi.org/https://doi.org/10.1002/2016RG000519, _eprint: https://agupubs.onlinelibrary.wiley.com/doi/pdf/10.1002/2016RG000519, 2016.

Clark, P. A. and Gray, S. L.: Sting jets in extratropical cyclones: a review, Quarterly Journal of the Royal Meteorological Society, 144, 943–969, https://doi.org/https://doi.org/10.1002/qj.3267, 2018.

Clark, P. A., Browning, K. A., and Wang, C.: The sting at the end of the tail: Model diagnostics of fine-scale three-dimensional structure of the cloud head, Quarterly Journal of the Royal Meteorological Society, 131, 2263–2292, https://doi.org/https://doi.org/10.1256/qj.04.36, 2005.

Colella, P. and Woodward, P. R.: The Piecewise Parabolic Method (PPM) for gas-dynamical simulations, Journal of Computational Physics, 54, 174 – 201, https://doi.org/https://doi.org/10.1016/0021-9991(84)90143-8, 1984.

Cuxart, J., Bougeault, P., and Redelsperger, J.-L.: A turbulence scheme allowing for mesoscale and large-eddy simulations, Quarterly Journal of the Royal Meteorological Society, 126, 1–30, https://doi.org/https://doi.org/10.1002/qj.49712656202, 2000.

Deardorff, J. W.: Stratocumulus-capped mixed layers derived from a three-dimensional model, Boundary-Layer Meteorology, 18, 495–527, https://doi.org/10.1007/BF00119502, 1980.

Edson, J. B., Jampana, V., Weller, R. A., Bigorre, S. P., Plueddemann, A. J., Fairall, C. W., Miller, S. D., Mahrt, L., Vickers, D., and Hersbach, H.: On the exchange of momentum over the open ocean, Journal of Physical Oceanography, 43, 1589–1610, https://doi.org/10.1175/JPO-D-12-0173.1, 2013.

Eisenstein, L., Pantillon, F., and Knippertz, P.: Dynamics of sting-jet storm Egon over continental Europe: Impact of surface properties and model resolution, Quarterly Journal of the Royal Meteorological Society, 146, 186–210, https://doi.org/10.1002/qj.3666, _eprint: https://rmets.onlinelibrary.wiley.com/doi/pdf/10.1002/qj.3666, 2020.

Escobar, J., Wautelet, P., Pianezze, J., Pantillon, F., Dauhut, T., Barthe, C., and Chaboureau, J.-P.: Porting the Meso-NH atmospheric model on different GPU architectures for the next generation of supercomputers (version MESONH-v55-OpenACC), Geoscientific Model Development, 18, 2679–2700, https://doi.org/10.5194/gmd-18-2679-2025, 2025.

Foltz, G. R., Zhang, D., Looney, L. B., Chiodi, A. M., Zhang, J. A., Zhang, C., Mazza, E., Chi, N.-H., and Cokelet, E. D.: Hurricane air-sea drag saturation and sea-state dependence revealed by surface drones, Science Advances, 12, eaec7422, https://doi.org/10.1126/sciadv.aec7422, 2026.

Gentile, E. S., Gray, S. L., Barlow, J. F., Lewis, H. W., and Edwards, J. M.: The Impact of Atmosphere-Ocean-Wave Coupling on the Near-Surface Wind Speed in Forecasts of Extratropical Cyclones, Boundary-Layer Meteorology, 180, 105–129, https://doi.org/10.1007/s10546-021-00614-4, 2021.

Gheusi, F. and Stein, J.: Lagrangian description of airflows using Eulerian passive tracers, Quarterly Journal of the Royal Meteorological Society, 128, 337–360, https://doi.org/10.1256/00359000260498914, 2002.

Ginesta, M., Yiou, P., Messori, G., and Faranda, D.: A methodology for attributing severe extratropical cyclones to climate change based on reanalysis data: the case study of storm Alex 2020, Climate Dynamics, 61, 229–253, https://doi.org/10.1007/s00382-022-06565-x, 2023.

Good, S., Fiedler, E., Mao, C., Martin, M. J., Maycock, A., Reid, R., Roberts-Jones, J., Searle, T., Waters, J., While, J., and Worsfold, M.: The Current Configuration of the OSTIA System for Operational Production of Foundation Sea Surface Temperature and Ice Concentration Analyses, Remote Sensing, 12, https://doi.org/10.3390/rs12040720, 2020.

Gray, S. L. and Volonté, A.: Extreme low-level wind jets in Storm Ciarán, Weather, 79, 384–389, https://doi.org/https://doi.org/10.1002/wea.7620, 2024.

Gray, S. L., Volonté, A., Martínez-Alvarado, O., and Harvey, B. J.: A global climatology of sting-jet extratropical cyclones, Weather and Climate Dynamics, 5, 1523–1544, https://doi.org/10.5194/wcd-5-1523-2024, publisher: Copernicus GmbH, 2024.

Gregory, D., Morcrette, J.-J., Jakob, C., Beljaars, A. M., and Stockdale, T.: Revision of convection, radiation and cloud schemes in the ECMWF model, Quart. J. Roy. Meteorol. Soc., 126, 1685–1710, https://doi.org/10.1002/qj.49712656607, 2000.

Heinze, R., Dipankar, A., Henken, C. C., Moseley, C., Sourdeval, O., Trömel, S., Xie, X., Adamidis, P., Ament, F., Baars, H., Barthlott, C., Behrendt, A., Blahak, U., Bley, S., Brdar, S., Brueck, M., Crewell, S., Deneke, H., Di Girolamo, P., Evaristo, R., Fischer, J., Frank, C., Friederichs, P., Göcke, T., Gorges, K., Hande, L., Hanke, M., Hansen, A., Hege, H.-C., Hoose, C., Jahns, T., Kalthoff, N., Klocke, D., Kneifel, S., Knippertz, P., Kuhn, A., van Laar, T., Macke, A., Maurer, V., Mayer, B., Meyer, C. I., Muppa, S. K., Neggers, R. A. J., Orlandi, E., Pantillon, F., Pospichal, B., Röber, N., Scheck, L., Seifert, A., Seifert, P., Senf, F., Siligam, P., Simmer, C., Steinke, S., Stevens, B., Wapler, K., Weniger, M., Wulfmeyer, V., Zängl, G., Zhang, D., and Quaas, J.: Large-eddy simulations over Germany using ICON: a comprehensive evaluation, Quarterly Journal of the Royal Meteorological Society, 143, 69–100, https://doi.org/10.1002/qj.2947, publisher: John Wiley & Sons, Ltd, 2017.

Hewson, T. D. and Neu, U.: Cyclones, windstorms and the IMILAST project, Tellus A: Dynamic Meteorology and Oceanography, 67, 27 128, https://doi.org/10.3402/tellusa.v67.27128, publisher: Taylor & Francis _eprint: https://doi.org/10.3402/tellusa.v67.27128, 2015.

https://doi.org/10.5194/egusphere-2026-4453
Preprint. Discussion started: 12 August 2026

Lac, C., Chaboureau, J.-P., Masson, V., Pinty, J.-P., Tulet, P., Escobar, J., Leriche, M., Barthe, C., Aouizerats, B., Augros, C., Aumond, P., Auguste, F., Bechtold, P., Berthet, S., Bielli, S., Bosseur, F., Caumont, O., Cohard, J.-M., Colin, J., Couvreux, F., Cuxart, J., Delautier, G., Dauhut, T., Ducrocq, V., Filippi, J.-B., Gazen, D., Geoffroy, O., Gheusi, F., Honnert, R., Lafore, J.-P., Lebeaupin Brossier, C., Libois, Q., Lunet, T., Mari, C., Maric, T., Mascart, P., Mogé, M., Molinié, G., Nuissier, O., Pantillon, F., Peyrillé, P., Pergaud, J., Perraud, E., Pianezze, J., Redelsperger, J.-L., Ricard, D., Richard, E., Riette, S., Rodier, Q., Schoetter, R., Seyfried, L., Stein, J., Suhre, K., Taufour, M., Thouron, O., Turner, S., Verrelle, A., Vié, B., Visentin, F., Vionnet, V., and Wautelet, P.: Overview of the Meso-NH model version 5.4 and its applications, Geoscientific Model Development, 11, 1929–1969, https://doi.org/10.5194/gmd-11-1929-2018, 2018.

Lfarh, W., Pantillon, F., and Chaboureau, J.-P.: The Downward Transport of Strong Wind by Convective Rolls in a Mediterranean Windstorm, Monthly Weather Review, 151, 2801 – 2817, https://doi.org/10.1175/MWR-D-23-0099.1, 2023.

Lfarh, W., Pantillon, F., Chaboureau, J.-P., and Brumer, S. E.: Impact of Surface Turbulent Fluxes on the Formation of Roll Vortices in a Mediterranean Windstorm, Journal of Geophysical Research: Atmospheres, 129, e2023JD040 191, https://doi.org/10.1029/2023JD040191, _eprint: https://onlinelibrary.wiley.com/doi/pdf/10.1029/2023JD040191, 2024.

Ludwig, P., Pinto, J. G., Hoepp, S. A., Fink, A. H., and Gray, S. L.: Secondary Cyclogenesis along an Occluded Front Leading to Damaging Wind Gusts: Windstorm Kyrill, January 2007, Monthly Weather Review, 143, 1417–1437, https://doi.org/10.1175/MWR-D-14-00304.1, publisher: American Meteorological Society, 2014.

Martínez-Alvarado, O., Gray, S. L., Hart, N. C. G., Clark, P. A., Hodges, K., and Roberts, M. J.: Increased wind risk from sting-jet windstorms with climate change, Environmental Research Letters, 13, 044 002, https://doi.org/10.1088/1748-9326/aaae3a, 2018.

Mass, C. and Dotson, B.: Major Extratropical Cyclones of the Northwest United States: Historical Review, Climatology, and Synoptic Environment, Monthly Weather Review, 138, 2499–2527, https://doi.org/10.1175/2010MWR3213.1, 2010.

Masson, V., Le Moigne, P., Martin, E., Faroux, S., Alias, A., Alkama, R., Belamari, S., Barbu, A., Boone, A., Bouyssel, F., Brousseau, P., Brun, E., Calvet, J.-C., Carrer, D., Decharme, B., Delire, C., Donier, S., Essaouini, K., Gibelin, A.-L., Giordani, H., Habets, F., Jidane, M., Kerdraon, G., Kourzeneva, E., Lafaysse, M., Lafont, S., Lebeaupin Brossier, C., Lemonsu, A., Mahfouf, J.-F., Marguinaud, P., Mokhtari, M., Morin, S., Pigeon, G., Salgado, R., Seity, Y., Taillefer, F., Tanguy, G., Tulet, P., Vincendon, B., Vionnet, V., and Voldoire, A.: The SURFEXv7.2 land and ocean surface platform for coupled or offline simulation of Earth surface variables and fluxes, Geoscientific Model Development, 6, 929–960, https://doi.org/10.5194/gmd-6-929-2013, 2013.

Maury, N., Pantillon, F., Brumer, S., Pianezze, J., Husson, R., and Mouche, A.: Complementarity between Large-Eddy Simulation and Synthetic-Aperture Radar observations to characterize surface wind in extratropical cyclone, Weather and Climate Dynamics, https://doi.org/10.5194/egusphere-2026-3679, 2026.

Minola, L., Zhang, F., Azorin-Molina, C., Pirooz, A. A. S., Flay, R. G. J., Hersbach, H., and Chen, D.: Near-surface mean and gust wind speeds in ERA5 across Sweden: towards an improved gust parametrization, Climate Dynamics, 55, 887–907, https://doi.org/10.1007/s00382-020-05302-6, 2020.

Pantillon, F., Mascart, P., Chaboureau, J.-P., Lac, C., Escobar, J., and Duron, J.: Seamless MESO-NH modeling over very large grids, Comptes Rendus Mécanique, 339, 136–140, https://doi.org/10.1016/j.crme.2010.12.002, 2011.

Pantillon, F., Lerch, S., Knippertz, P., and Corsmeier, U.: Forecasting wind gusts in winter storms using a calibrated convection-permitting ensemble, Quarterly Journal of the Royal Meteorological Society, 144, 1864–1881, https://doi.org/10.1002/qj.3380, _eprint: https://rmets.onlinelibrary.wiley.com/doi/pdf/10.1002/qj.3380, 2018.

https://doi.org/10.5194/egusphere-2026-4453
Preprint. Discussion started: 12 August 2026

Pantillon, F., Adler, B., Corsmeier, U., Knippertz, P., Wieser, A., and Hansen, A.: Formation of Wind Gusts in an Extratropical Cyclone in Light of Doppler Lidar Observations and Large-Eddy Simulations, Monthly Weather Review, 148, 353–375, https://doi.org/10.1175/MWR-D-19-0241.1, publisher: American Meteorological Society, 2020.

Pergaud, J., Masson, V., Malardel, S., and Couvreux, F.: A Parameterization of Dry Thermals and Shallow Cumuli for Mesoscale Numerical Weather Prediction, Boundary-Layer Meteorology, 132, 83–106, https://doi.org/10.1007/s10546-009-9388-0, 2009.

Pianezze, J., Barthe, C., Bielli, S., Tulet, P., Jullien, S., Cambon, G., Bousquet, O., Claeys, M., and Cordier, E.: A New Coupled Ocean-Waves-Atmosphere Model Designed for Tropical Storm Studies: Example of Tropical Cyclone Bejisa (2013-2014) in the South-West Indian Ocean, spray, Journal of Advances in Modeling Earth Systems, 10, 801–825, https://doi.org/10.1002/2017MS001177, 2018.

Pineau-Guillou, L., Ardhuin, F., Bouin, M.-N., Redelsperger, J.-L., Chapron, B., Bidlot, J.-R., and Quilfen, Y.: Strong winds in a coupled wave–atmosphere model during a North Atlantic storm event: evaluation against observations, Quarterly Journal of the Royal Meteorological Society, 144, 317–332, https://doi.org/10.1002/qj.3205, _eprint: https://rmets.onlinelibrary.wiley.com/doi/pdf/10.1002/qj.3205, 2018.

Pinto, J. G., Pantillon, F., Ludwig, P., Déroche, M.-S., Leoncini, G., Raible, C. C., Shaffrey, L. C., and Stephenson, D. B.: From Atmospheric Dynamics to Insurance Losses – an Interdisciplinary Workshop on European Storms, Bulletin of the American Meteorological Society, pp. BAMS–D–19–0026.1, https://doi.org/10.1175/BAMS-D-19-0026.1, 2019.

Pinty, J.-P. and Jabouille, P.: A mixed-phase cloud parameterization for use in a mesoscale non-hydrostatic model: simulations of a squall line and of orographic precipitation, in: Proc. Conf. of Cloud Physics, edited by Amer. Meteor. soc., pp. 217 – 220, Everett, WA, USA, http://mesonh.aero.obs-mip.fr/mesonh/dir_publication/pinty_jabouille_ams_ccp1998.pdf, 1998.

Potter, H., Collins, C. O., Drennan, W. M., and Graber, H. C.: Observations of wind stress direction during Typhoon Chaba (2010)., Geophysical Research Letters, 42, 9898–9905, https://doi.org/10.1002/2015GL065173, 2015.

Quinting, J., Grams, C. M., Kirsch, B., Oertel, A., Ramos, A. M., Raveh-Rubin, S., and Schäfler, A.: Dry intrusion connects high-impact cyclones Eunice and Franklin: emerging observational targets of NAWDIC, Bulletin of the American Meteorological Society, pp. BAMS–D–25–0170.1, https://doi.org/10.1175/BAMS-D-25-0170.1, 2026.

Raveh-Rubin, S.: Dry Intrusions: Lagrangian Climatology and Dynamical Impact on the Planetary Boundary Layer, Journal of Climate, 30, 6661 – 6682, https://doi.org/10.1175/JCLI-D-16-0782.1, 2017.

Rivière, G., Delanoë, J., Pantillon, F., Ricard, D., Planche, C., Coutris, P., and Sodemann, H.: La campagne Nawdic sur les tempêtes hivernales, La Météorologie, 2026, 4–7, 2026.

Rivière, G., Ricard, D., and Arbogast, P.: The downward transport of momentum to the surface in idealized sting-jet cyclones, Quarterly Journal of the Royal Meteorological Society, 146, 1801–1821, https://doi.org/https://doi.org/10.1002/qj.3767, 2020.

Saunders, R., Hocking, J., Turner, E., Rayer, P., Rundle, D., Brunel, P., Vidot, J., Roquet, P., Matricardi, M., Geer, A., Bormann, N., and Lupu, C.: An update on the RTTOV fast radiative transfer model (currently at version 12), Geoscientific Model Development, 11, 2717–2737, https://doi.org/10.5194/gmd-11-2717-2018, 2018.

Schultz, D. M.: Reexamining the Cold Conveyor Belt, Monthly Weather Review, 129, 2205 – 2225, https://doi.org/10.1175/1520-0493(2001)129<2205:RTCCB>2.0.CO;2, 2001.

Schultz, D. M. and Sienkiewicz, J. M.: Using Frontogenesis to Identify Sting Jets in Extratropical Cyclones, Weather and Forecasting, 28, 603–613, https://doi.org/10.1175/WAF-D-12-00126.1, publisher: American Meteorological Society Section: Weather and Forecasting, 2013.

https://doi.org/10.5194/egusphere-2026-4453
Preprint. Discussion started: 12 August 2026

Schultz, D. M., Bosart, L. F., Colle, B. A., Davies, H. C., Dearden, C., Keyser, D., Martius, O., Roebber, P. J., Steenburgh, W. J., Volkert, H., and Winters, A. C.: Extratropical Cyclones: A Century of Research on Meteorology's Centerpiece, Meteorological Monographs, 59, 16.1–16.56, https://doi.org/10.1175/AMSMONOGRAPHS-D-18-0015.1, 2018.

Seity, Y., Brousseau, P., Malardel, S., Hello, G., Bénard, P., Bouttier, F., Lac, C., and Masson, V.: The AROME-France Convective-Scale Operational Model, Monthly Weather Review, 139, 976 – 991, https://doi.org/10.1175/2010MWR3425.1, 2011.

Sheridan, P.: Current gust forecasting techniques, developments and challenges, in: Advances in Science and Research, vol. 15, pp. 159–172, Copernicus GmbH, https://doi.org/https://doi.org/10.5194/asr-15-159-2018, 2018.

Suri, D., Keates, S., and Sidaway, M.: Storm Éowyn, 24 January 2025, Weather, 80, 228–231, https://doi.org/https://doi.org/10.1002/wea.7725, 2025.

Terray, L. and Bador, M.: Influence of large-scale atmospheric circulation and Mediterranean sea surface temperature to extreme land precipitation: the case of storm Alex, Environmental Research: Climate, 4, 015 002, https://doi.org/10.1088/2752-5295/adaa0d, publisher: IOP Publishing, 2025.

The WAVEWATCH III® Development Group: User manual and system documentation of WAVEWATCH III® version 5.16, Tech. Rep. 329, NOAA/NWS/NCEP/MMAB, College Park, MD, USA, 326 pp. + Appendices, 2016.

Voldoire, A., Decharme, B., Pianezze, J., Lebeaupin Brossier, C., Sevault, F., Seyfried, L., Garnier, V., Bielli, S., Valcke, S., Alias, A., Accensi, M., Ardhuin, F., Bouin, M.-N., Ducrocq, V., Faroux, S., Giordani, H., Léger, F., Marsaleix, P., Rainaud, R., Redelsperger, J.-L., Richard, E., and Riette, S.: SURFEX v8.0 interface with OASIS3-MCT to couple atmosphere with hydrology, ocean, waves and sea-ice models, from coastal to global scales, Geoscientific Model Development, 10, 4207–4227, https://doi.org/10.5194/gmd-10-4207-2017, 2017.

Volonté, A., Joos, H., Lee, M. H. F., Forbes, R. M., and Bouffet-Klein, R.: Identifying the diabatic processes driving the evolution of a sting jet: the case of Storm Ciarán, EGUsphere, preprint, 1–36, https://doi.org/10.5194/egusphere-2025-5225, 2025.

Volonté, A., Clark, P. A., and Gray, S. L.: The role of mesoscale instabilities in the sting-jet dynamics of windstorm Tini, Quarterly Journal of the Royal Meteorological Society, 144, 877–899, https://doi.org/10.1002/qj.3264, _eprint: https://onlinelibrary.wiley.com/doi/pdf/10.1002/qj.3264, 2018.

Volonté, A., Gray, S. L., Clark, P. A., Martínez-Alvarado, O., and Ackerley, D.: Strong surface winds in Storm Eunice. Part 1: storm overview and indications of sting jet activity from observations and model data, Weather, 79, 40–45, https://doi.org/https://doi.org/10.1002/wea.4402, 2024a.

Volonté, A., Gray, S. L., Clark, P. A., Martínez-Alvarado, O., and Ackerley, D.: Strong surface winds in Storm Eunice. Part 2: airstream analysis, Weather, 79, 54–59, https://doi.org/https://doi.org/10.1002/wea.4401, 2024b.

Watchers, T.: Death toll caused by storm Alex rises to 15, 21 still missing in France and Italy, https://watchers.news/2020/10/86907/storm-alex-death-toll-damage-october2020/, 2020.

World Meteorological Organization: Guide to Instruments and Methods of Observation (WMO-No. 8), WMO, Geneva, ISBN 978-92-63-10008-5, 2018.

Zappa, C. J., Brown, S. M., Laxague, N. J. M., Dhakal, T., Harris, R. A., Farber, A. M., and Subramaniam, A.: Using Ship-Deployed High-Endurance Unmanned Aerial Vehicles for the Study of Ocean Surface and Atmospheric Boundary Layer Processes, Frontiers in Marine Science, 6, https://doi.org/10.3389/fmars.2019.00777, 2020.

https://doi.org/10.5194/egusphere-2026-4453
Preprint. Discussion started: 12 August 2026

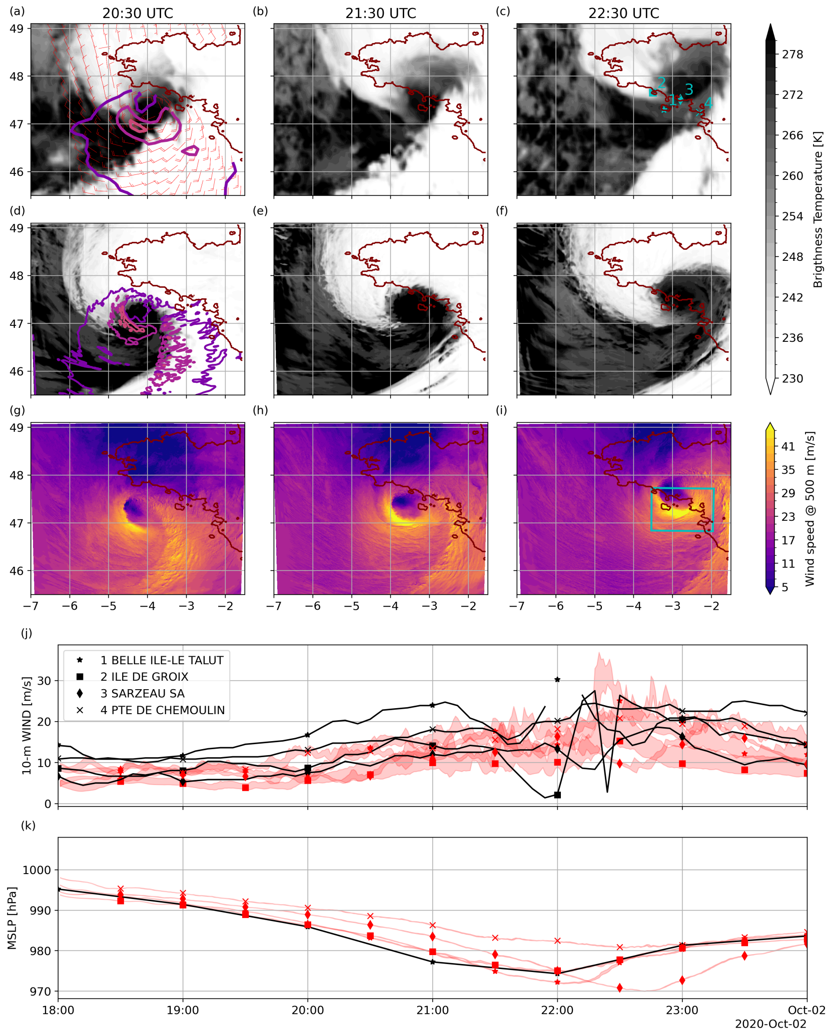

Figure 1. Maps for three consecutive hours on October 1st (20:30 UTC, 21:30 UTC, and 22:30 UTC) of (a-c) the measured MSG SEVIRI brightness temperature (infrared 10.8 μm channel), (d-f) the simulated brightness temperature in A1600, and (g-i) the horizontal wind speed at 500 m altitude (model level 16) in the A200 simulation. Overlay on (d) are contours and wind barbs of the ASCAT derived 10 m wind speed (15, 20, and 25 $\mathrm{m\,s^{-1}}$) and direction and on (g) contours of the simulated 10 m wind speed from A1600. The square in (i) delimits the region of interest for the trajectory analysis. Shown in (c) are the locations of 4 coastal stations which provided timeseries of the 10-m equivalent winds at a temporal resolution of 6 minutes shown in (j). The station on Belle-Île also provided hourly sea level pressure record whose timeseries is plotted in (k). The red lines in (j) and (k) show corresponding output (shading between the 25$^{\mathrm{th}}$ and 75$^{\mathrm{th}}$ percentiles) of the A200 simulation within a 2 km radius of the stations.

https://doi.org/10.5194/egusphere-2026-4453
Preprint. Discussion started: 12 August 2026

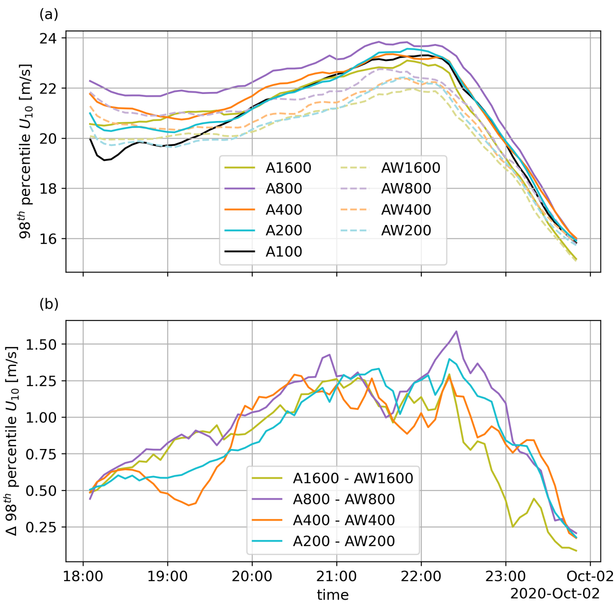

Figure 2. Timeseries of (a) the 98$^{\text{th}}$ percentile of the 10-m wind speed of all simulations and (b) the difference of the 98$^{\text{th}}$ percentile of the 10-m wind speed in simulations with minus without wave coupling. In (a) solid lines correspond to the atmosphere only runs and dashed lines to the coupled wave-atmosphere runs, where each color pair corresponds to a horizontal grid resolution. Only values over the sea are included in the percentile calculation.

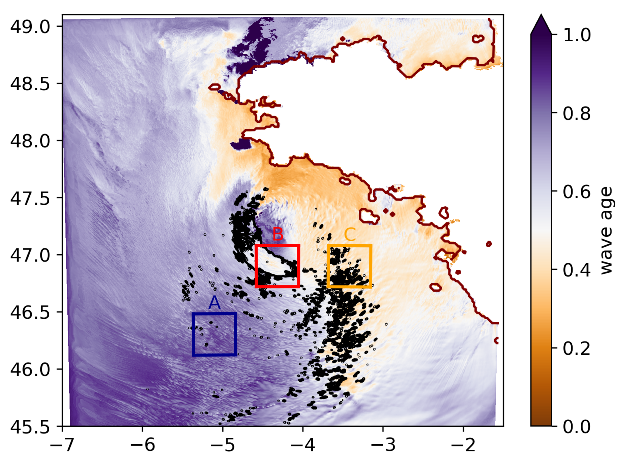

Figure 3. Map showing the wave age ω_{ws} computed in the coupled simulation AW200 at 20:30 UTC. Orange and purple tones indicate where the waves are younger and older, respectively, than the default in the uncoupled simulation A200 where the wave age is assumed to be equal to 0.5. The black contours demarcates the region where the 10-m winds exceed 22 $\mathrm{m\,s^{-1}}$ in A200. The three colored squares A, B, and C demarcate 40×40 km^2 regions with contrasting wave impacts which are detailed further in Fig. 4 .

https://doi.org/10.5194/egusphere-2026-4453
Preprint. Discussion started: 12 August 2026

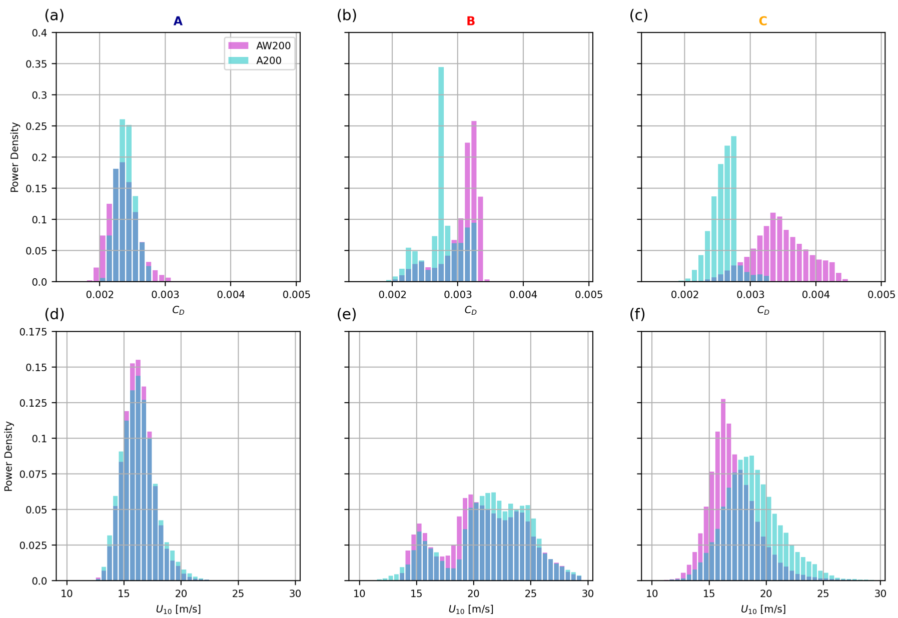

Figure 4. Power density distributions of (a–c) the drag coefficient C_D and (d–f) the 10-m winds U_{10} in the three boxes A, B, and C shown in Fig. 3: where waves are younger (a, d), older (c, f), and a mixture of younger and older (b, e) in the coupled simulation AW200 (purple bars) than assumed in the atmosphere only simulation A200 (cyan bars). The region where they overlap is in blue.

https://doi.org/10.5194/egusphere-2026-4453
Preprint. Discussion started: 12 August 2026

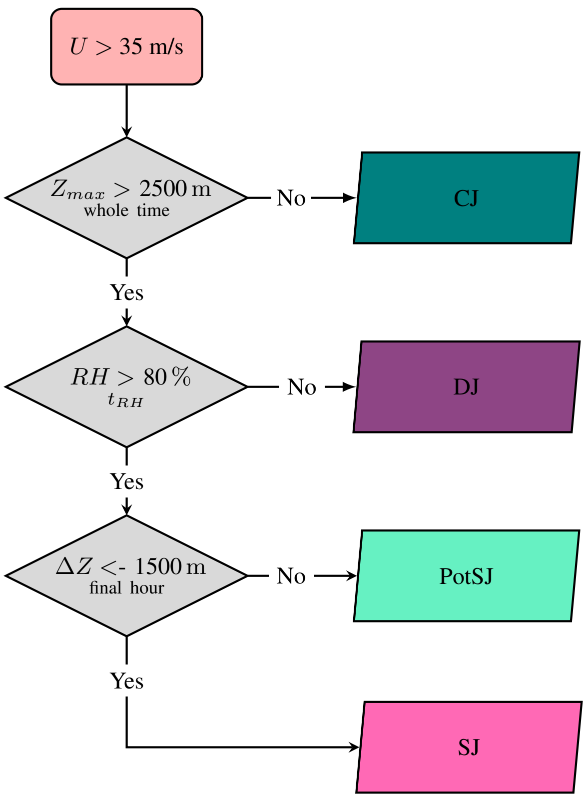

Figure 5. Flowchart of the method used to distinguish jets responsible for the strong wind (U>35 m s^{-1}).

https://doi.org/10.5194/egusphere-2026-4453
Preprint. Discussion started: 12 August 2026

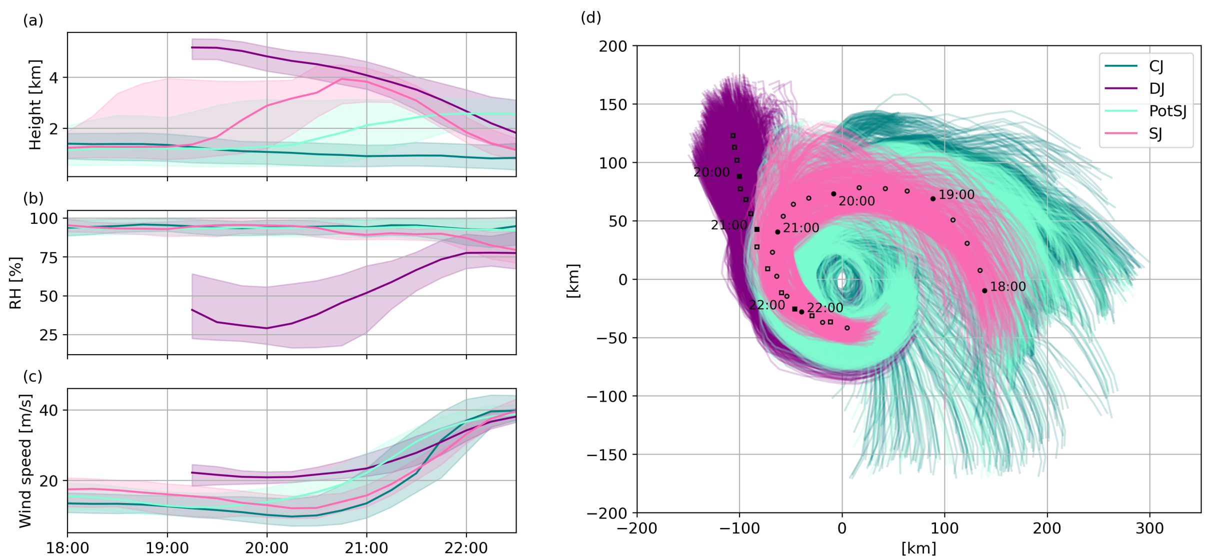

Figure 6. Time evolution (median in solid lines and 25th and 75th percentiles shaded) of height (a), relative humidity (b), and wind speed (c), and cyclone-relative position (d) along trajectories from A1600 responsible for the strongest horizontal winds (above 35 $\mathrm{m\,s^{-1}}$) between the surface and 4250 m altitude at 22:30 UTC on October 1 (square in Fig. 1(i)) associated to the Cold Jet (CJ, green), the Sting Jet (SJ, pink), the potential SJ (PotSJ, turquoise), and the Dry Jet (DJ, purple). Dots and squares on (d) show the median location of the SJ and DJ. DJ timeseries data and position markers prior to 19:15 UTC are omitted due to the fact that a significant number of trajectories could not be reconstructed that far back as they originated from outside of the simulation domain.

https://doi.org/10.5194/egusphere-2026-4453
Preprint. Discussion started: 12 August 2026

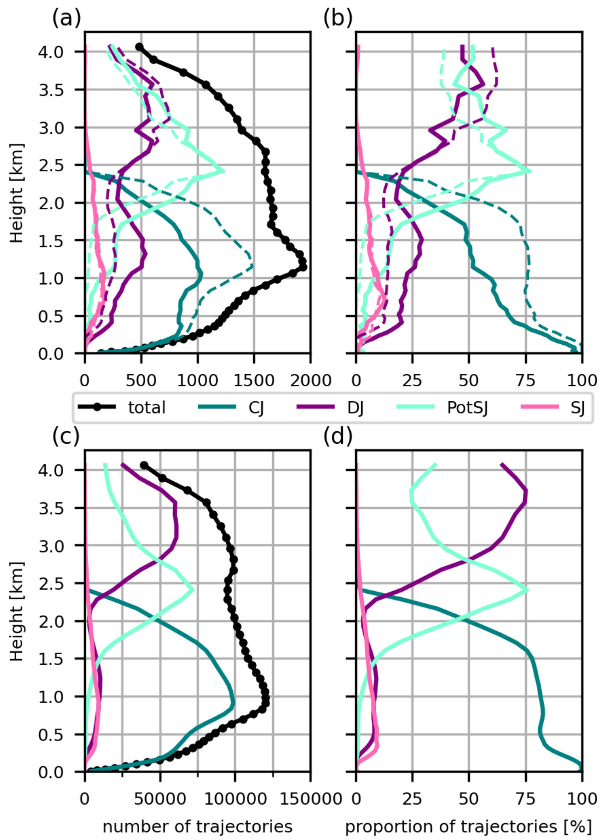

Figure 7. Vertical distribution of filtered trajectories with final horizontal winds greater than 35 $\mathrm{m\,s^{-1}}$ in the A1600 (a, b) and A200 (c, d) simulations for each jet expressed as numbers per level (a, c), and percentages of total per level (b, d). Solid lines in (a,b) result from applying classification criteria to the whole time of trajectory reconstruction and dashed lines result from applying them only to the last hour. Jets are color-coded as follows: Cold Jet (CJ, green), Sting Jet (SJ, pink), potential SJ (PotSJ, turquoise), and the Dry Jet (DJ, purple). The analysis of A1600 includes around 60 000 high wind trajectories and that of A200 around 4 million.

https://doi.org/10.5194/egusphere-2026-4453
Preprint. Discussion started: 12 August 2026

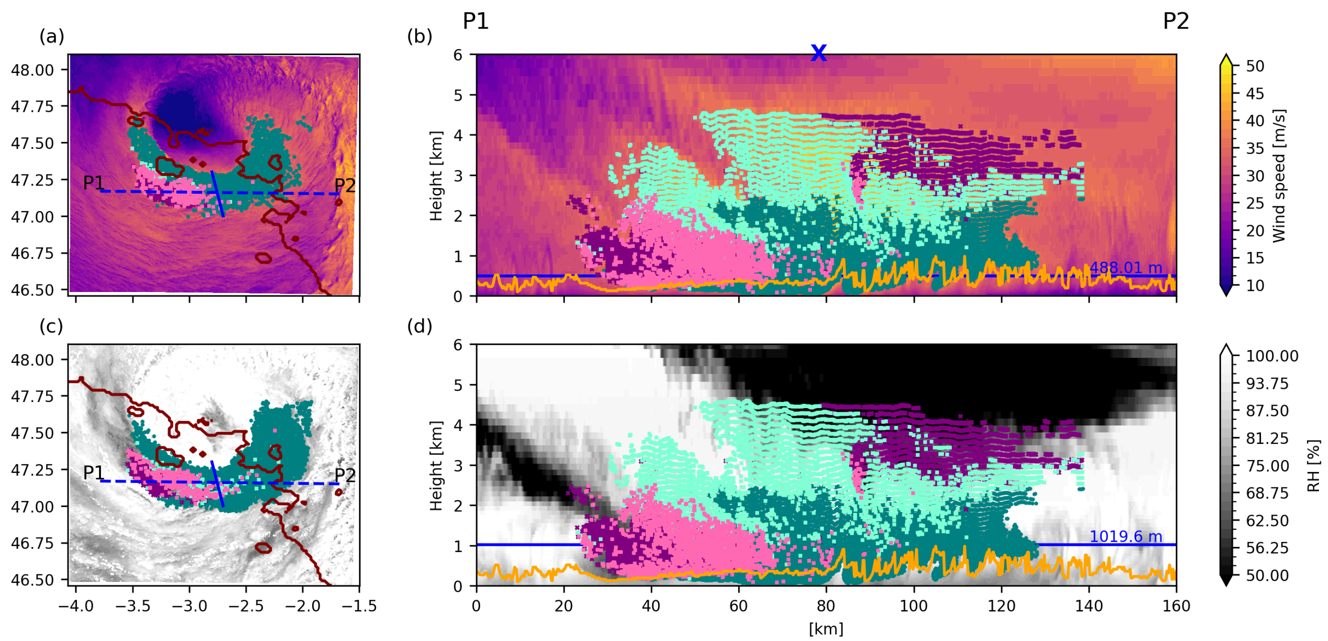

Figure 8. Maps and vertical cross sections of (a,b) the horizontal wind speed, and (c,d) the relative humidity from the A200 output on October 1st at 22:30. The zonal cross section spans P1–P2 shown in the maps crossing the high wind core at 47.1°N (dashed line). Colored dots show the geographic distribution of air parcels corresponding to the different jets: the Cold Jet (CJ, green), the Sting Jet (SJ, pink), the potential SJ (PotSJ, turquoise), and the Dry Jet (DJ, purple). Two different altitudes are shown in the maps: ≈500 m for the horizontal winds (a) and ≈1000 m for the relative humidity (c). These are marked by the horizontal blue line in the corresponding cross sections. The orange line in (b) indicates the height of the marine atmospheric boundary layer. The blue cross at the top of the cross section (b) indicates the location of the cross section depicted in Fig. 9 along the solid blue line shown in the maps.

https://doi.org/10.5194/egusphere-2026-4453
Preprint. Discussion started: 12 August 2026

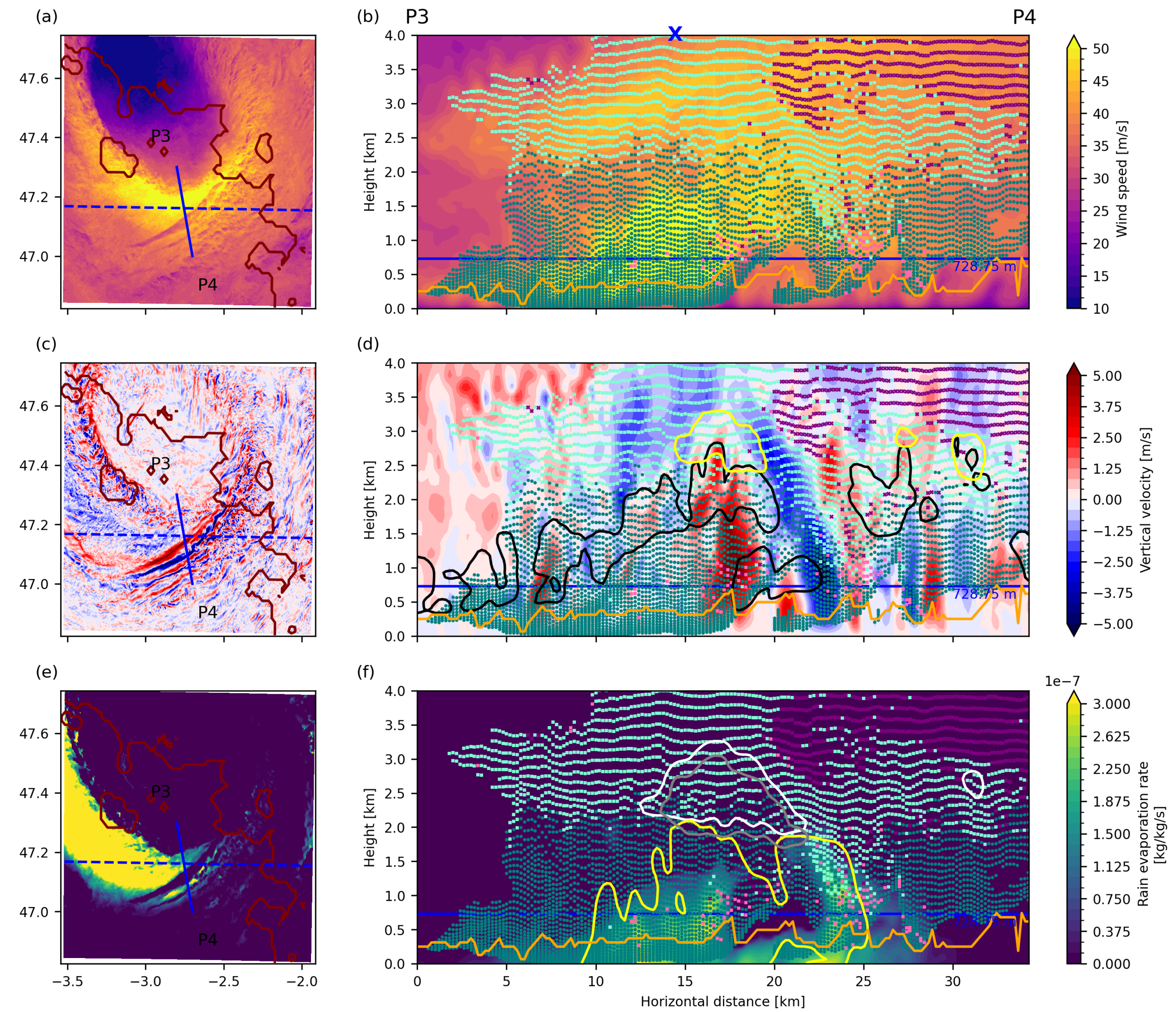

Figure 9. Maps and vertical cross sections of (a, b) the horizontal wind speed, (c,d) the vertical wind speed, and (e,f) the evaporation rate from the A200 output on October 1st at 22:30. The cross-sections are along P3–P4 (solid blue line in the maps) roughly perpendicular to the horizontal winds in the leading edge of the strong wind core. The dots represent the position of the trajectories corresponding to the Cold Jet (CJ, green), the Sting Jet (SJ, pink), the potential SJ (PotSJ, turquoise), and the Dry Jet (DJ, purple). The maps show output at ≈700 m as marked by the horizontal blue line in the corresponding cross sections. The orange line in the cross sections indicates the height of the marine atmospheric boundary layer. Contours in (d) highlight where the mixing ratios of non-precipitable hydrometeors (black for cloud water, yellow for ice) exceed 10^{-4} kg kg^{-1}. Contours in (f) highlight where the precipitable hydrometeors mixing ratios (yellow for rain, white for graupel, and grey for snow) exceed 10^{-4} kg kg^{-1}. The blue cross at the top of the cross section (b) indicates the location of the cross section depicted in Fig. 8 along the dashed blue line shown in the maps